Document Version
Final published version

Licence
CC BY

Citation (APA)
Altenburg, L. A., Klein, S. A., & Tummers, M. J. (2026). Stabilization of premixed hydrogen–air flames in a trapped vortex combustor. *International Journal of Hydrogen Energy*, *208*, Article 153469.
https://doi.org/10.1016/j.ijhydene.2026.153469

International Journal of Hydrogen Energy 208 (2026) 153469

Contents lists available at ScienceDirect

International Journal of Hydrogen Energy

journal homepage: www.elsevier.com/locate/he

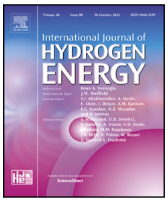

Stabilization of premixed hydrogen–air flames in a trapped vortex combustor

Luuk A. Altenburg *, Sikke A. Klein, Mark J. Tummers

Department of Process & Energy (P&E), Delft University of Technology, Leeghwaterstraat 39, 2628 CB Delft, The Netherlands

ARTICLE INFO

Keywords:
Hydrogen combustion
FlameSheet™ technology
Turbulent premixed flames
Boundary layer flashback
Strained flames

ABSTRACT

This study investigates flame stabilization and flashback in a trapped vortex combustor operating on a lean premixed hydrogen–air mixture at an equivalence ratio of $\phi = 0.35$. The combustor geometry features a U-bend in conjuction with a liner plate that aerodynamically stabilizes the flame. Particle Image Velocimetry (PIV) was used to study the (reacting) flow in detail at two Reynolds numbers: $Re = 9.68 \times 10^3$ (case R-1, marginally stable flame) and $Re = 13.55 \times 10^3$ (case R-2, highly stable flame). Within the U-bend, the flame front shows steady laminar-like behaviour where the velocity is primarily tangential to the flame front. Downstream of the U-bend, the shear layer weakens and the flame front becomes more intermittent. This intermittency may cause flame bulges to reach low-velocity zones near the U-bend wall, increasing the possibility of flame flashback through the boundary layer that wall. An analysis of the strain rate tensor shows that within the U-bend, the angle between the flame front normal and the most extensive strain rate direction remains close to 45°, indicating the dominance of shear straining in this region. Further downstream, alignment with the most extensive strain rate increases, indicating that combustion-induced expansion becomes more dominant.

1. Introduction

Electricity generation using gas turbines depends heavily on natural gas. However, the push for cleaner energy sources has put hydrogen in the spotlight as a promising alternative. It obviously produces no carbon dioxide and, when burned in a lean mixture, has very low NOx emissions. However, switching from natural gas to hydrogen comes with challenges, because lean premixed hydrogen flames generally have a much higher effective flame speed in comparison to premixed natural gas flames. This is due to a combination of increased laminar flame speed and the thermo-diffusive instability, which is the combined effect of the nonunity Lewis number and the preferential diffusion effect that occurs in lean premixed hydrogen flames due to the high mass diffusivity of hydrogen [1]. This poses a challenge in the design of gas turbine combustion systems that run on hydrogen in lean premixed mode. One significant issue is flame flashback, where the flame propagates upstream into parts of the burner that are not designed to handle high temperatures, leading to potential damage and safety concerns [2]. An important mechanism of flashback in high hydrogen-fired gas turbines is boundary layer flashback, which occurs when flames propagate upstream due to the low flow velocities in the near-wall regions. The low-speed streaks in the boundary layer impact the local flame front curvature, which, in turn, triggers the thermo-diffusive instability that results in a local enrichment of the flame and therefore an increase in flame speed in lean premixed hydrogen combustion [3]. To improve flame stabilization and mitigate flashback risks in lean premixed hydrogen combustion, new combustor technologies are developed. One such technology is the FlameSheet™ combustor which relies on stabilization of the premixed flame by means of a trapped vortex that recirculates hot combustion products thus providing a continuous ignition source. The FlameSheet™ combustor showed excellent performance with high hydrogen content fuels [4], but flashback still poses a problem for lean combustion with 100% hydrogen.

The current study investigates a trapped vortex combustor using optical measurement techniques to capture the flame–flow interaction. The combustor design is inspired by the FlameSheet combustor, which features an axisymmetric 180-degree turn of the flow direction (U-bend) around the tip of an inner liner [5], see Fig. 1. In this design, the fuel–air mixture entering the combustor separates at the combustion liner tip and thus forms a trapped vortex which stabilizes the flame. Additionally, the flow field disrupts the turbulent boundary layer along the U-bend wall, making flashback through this boundary layer more likely. Four aspects of the trapped vortex combustor design that dictate the flow field are the shape of the U-bend, the shape of the inner liner tip, the position of the liner with respect to the U-bend and the ratio between the channel height before and after the U-bend. These aspects were simplified in this study to create a more feasible academic investigation. Due to the challenges associated with using

---

* Corresponding author.
E-mail address: l.a.altenburg@tudelft.nl (L.A. Altenburg).

https://doi.org/10.1016/j.ijhydene.2026.153469
Received 3 October 2025; Received in revised form 26 December 2025; Accepted 8 January 2026

Nomenclature

Abbreviations

MFC	Mass Flow Controller
PIV	Particle Image Velocimetry
PSD	Power Spectral Density

Greek Symbols

δ_L	thermal laminar flame thickness
ε	turbulent dissipation rate
λ_1	most extensive strain rate
λ_2	most compressive strain rate
ν_u	kinematic viscosity of the unburnt mixture
τ_η	Kolmogorov time scale
τ_L	flame time scale
τ_t	turbulent time scale
ϕ	equivalence ratio
ω	vorticity

Latin Symbols

$\mathbf{e}_1$	eigenvector of the most extensive strain rate
$\mathbf{e}_2$	eigenvector of the most compressive strain rate
$\mathbf{n}$	unit vector normal to the flame front
$\mathbf{S}$	strain rate tensor
$\mathbf{u}$	velocity vector
c_f	curve defining the average flame front location
D_H	hydraulic diameter of the channel
$d_i(x, y)$	spatial coordinate along line i
Da	Damköhler number
h_1	main-flow inlet channel height
h_2	confinement height downstream of the U-bend
h_3	co-flow inlet channel height
k	turbulent kinetic energy
Ka	Karlovitz number
L_f	length of curve c_f
L_i	length of line i
l_o	integral length scale
Le	Lewis number
Re	Reynolds number based on hydraulic diameter
S_{L0}	unstretched laminar flame speed
T_b	burnt mixture temperature
T_u	unburnt mixture temperature
u	velocity component
U_b	bulk velocity of the main-flow inlet
u'_o	turbulent velocity fluctuations
x	streamwise coordinate
y	coordinate normal to (top face of) liner wall
z	spanwise coordinate
$H_2\%$	volume percentage of hydrogen in the fuel

Subscripts and superscripts

$(.)''$	Favre fluctuation
$(.)^*$	dimensionless quantity
$(.)_\perp$	component perpendicular to line
$(.)_n$	normal component
$(.)_t$	tangential component
$(.)_x$	component in x-direction
$(.)_y$	component in y-direction
$(.)_{fb}$	flashback
$\widetilde{(.)}$	Favre-averaged quantity

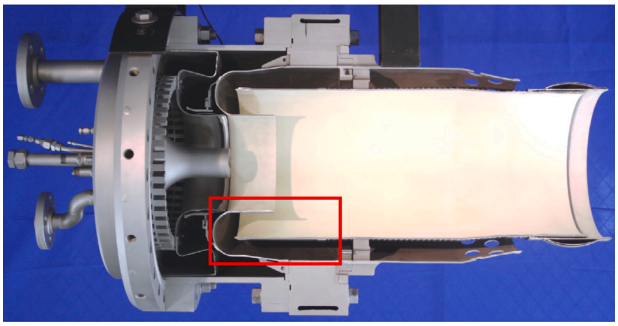

Fig. 1. A cutaway view of the FlameSheet™ combustor. The red rectangle highlights the U-bend and the inner liner, which is the geometry of interest in present study.

optical diagnostics to investigate an axisymmetric combustor, a planar version of the trapped vortex combustor was used in this study. Particle Image Velocimetry (PIV) and related Mie-scattering measurements were employed to investigate the flame–flow interaction of a lean premixed hydrogen–air mixture for two Reynolds numbers: one for a highly stable flame and one marginally stable flame. It is important to realize that both investigated flames (“highly stable” and “marginally stable”) are stable flames, but the latter is closer to flashback than the former.

The main objective of this study is to experimentally investigate the complex turbulent flow field and the interaction between the local flame front and the underlying strain field in a planar trapped vortex combustor operating with a lean premixed hydrogen–air mixture under stable flame conditions and conditions near flashback. The structure of this paper is as follows: Section 2 discusses the experimental and diagnostic setup. Section 3 outlines the methods employed to investigate the interaction between the flame and the flow. Section 4 presents the results, and Section 5 presents the main conclusions of this study.

2. Experimental setup

2.1. Combustor and flame conditions

The relevant dimensions of the trapped vortex combustor and the nomenclature used in the present study are shown in Fig. 2. All parts of the combustor are made of ceramic glass, except for the U-bend, which consists of a single piece of quartz glass. The combustor has a main-flow and a co-flow inlet corresponding to the main reactants flow and the air co-flow. Both inlets have a height $h_1 = h_3 = 10\,\mathrm{mm}$ and a span-wise width of 300 mm. Downstream of the U-bend, the flow confinement height is $h_2 = 30\,\mathrm{mm}$. The combustor has an inner liner with a blunt-shaped (rectangular) tip. The x, y, z-coordinate system has its origin at the tip of the inner liner plate with the x-axis along the liner plate (top) surface. The y-axis is normal to the (top) surface of the inner liner plate and the z-axis is in the spanwise direction. The tip of the inner liner plate is positioned in the x-direction at the start of the U-bend. Fig. 2 also features colored dashed lines, which represent the locations where velocity statistics were extracted from the PIV data.

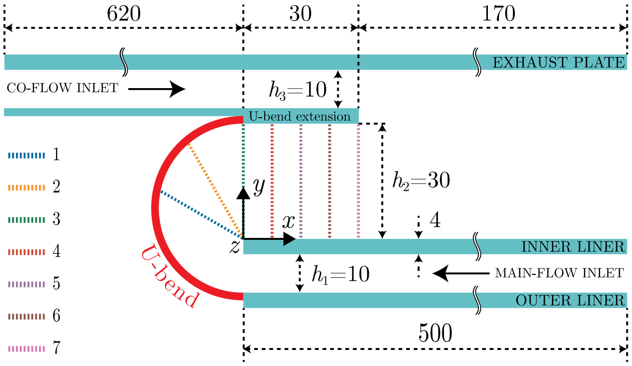

Fig. 2. Cross-sectional view of the trapped vortex combustor. The dimensions are in mm. The x, y, z-coordinate system has its origin at the tip of the inner liner plate with the x-axis along the liner plate (top) surface. The y-axis is normal to the (top) surface of the inner liner plate and the z-axis is in the spanwise direction. The colored dashed lines (1–7) represent the locations where velocity statistics from PIV data were extracted. All profile lines start at the inner liner (tip), with the blue (line 1) and orange (line 2) profile lines oriented at 60° and 30° to the positive y-axis, respectively.

All profile lines start at the inner liner (tip), with the blue and orange profile lines oriented at 60° and 30° to the positive y-axis, respectively.

Hydrogen and air are premixed 2 m upstream of the liner tip to ensure that a fully homogeneous H_2-air mixture reaches the flame-stabilization location. In order to control the main flow (hydrogen and air) and co-flow (air only) three mass flow controllers (MFCs) are employed. The MFCs are controlled using a LabView control panel in which three parameters are specified, i.e. the Reynolds number (Re), the equivalence ratio (ϕ) and the volume percentage of hydrogen in the fuel (H_2%). The Reynolds number is based on the hydraulic diameter of the main-flow inlet D_H, the bulk velocity in the main-flow inlet (U_b) and the kinematic viscosity of the unburnt mixture (ν_u). The bulk velocity is calculated from the MFC readings, which are corrected for standard pressure and standard temperature, and the cross-sectional area of the main-flow inlet channel. The streamwise lengths of the main-flow and co-flow channels are 0.5 m and 0.62 m, respectively, to ensure fully developed turbulent flow. Based on the maximum Reynolds number in this study, $Re = 13.55 \times 10^3$, fully developed turbulence is assumed according to the criterion $L_e/D_H = 1.359 Re^{1/4} \approx 15$, where L_e is the entrance length [6]. For the main-flow inlet, $L/D_H \approx 25$, which satisfies this criterion to achieve a fully developed turbulent flow.

Experiments were conducted for a lean H_2-air mixture at an equivalence ratio $\phi = 0.35$ for two Reynolds numbers $Re = 9.68 \times 10^3$ and $Re = 13.55 \times 10^3$. This equivalence ratio was chosen because it represents typical operating conditions of a high hydrogen-fired gas turbine. The co-flow is chosen to match the Reynolds number of the main flow. A flashback experiment was conducted to find the flashback limit of the investigated mixture in this combustor. Flashback was induced by decreasing the Reynolds number (bulk velocity) incrementally while keeping the mixture properties constant. From a total of 18 flashback experiments, the Reynolds number values at flashback Re_{fb} were found to range from 8.52×10^3 to 9.48×10^3. The average Reynolds number at flashback was determined to be $Re_{fb} = 8.98 \times 10^3$. Consequently, the two Reynolds numbers considered in this study, i.e., $Re = 9.68 \times 10^3$ and $Re = 13.55 \times 10^3$, are 7.8% and 51% above the average flashback limit, respectively. The former is referred to as the "marginally stable flame" condition, whereas the latter is referred to as the "highly stable flame" condition. More details of the cases considered in this study are given in Table 1, where 'NR' represents a non-reacting case and 'R' refers to a reacting case.

Table 1
Specification of the four cases considered in this study.

Case	Re	U_b (m s^{-1})	ϕ	H_2%	Stable condition
NR-1	9.68×10^3	7.44	–	0	–
NR-2	13.55×10^3	10.33	–	0	–
R-1	9.68×10^3	8.57	0.35	100	marginally
R-2	13.55×10^3	11.88	0.35	100	highly

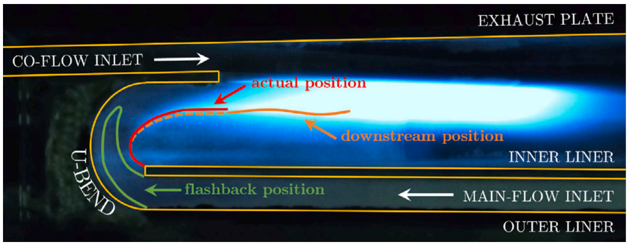

Fig. 3. The time-averaged (averaged over 300 images that were recorded at a frame rate of 60 Hz) image of the flame ($\phi = 0.4$, H_2%=80, $Re = 11.61 \times 10^3$), with the three potential flame positions: flashback position (green line), actual position (red line) and downstream position (orange line).

2.2. Diagnostic setup

Particle Image Velocimetry (PIV) was used to obtain quantitative and qualitative data on the velocity fields. The air flow of the main-flow inlet is seeded with aluminum-oxide particles (Al_2O_3) with a mean diameter of approximately 1 μm. Particles of this size are sufficiently small to accurately follow the flow [7]. A Nd:YLF dual-cavity laser (Quantronix Darwin-Duo Pro527-80-M) emitting a beam of green light (at 527 nm wavelength) was used to illuminate the particles. The laser beam is transformed into a laser sheet with a waist of approximately 1 mm using a system of plano-concave and convex lenses. The illuminated particles were imaged on the 12-bit CMOS sensor of a Photron Fastcam SA1.1 high-speed camera fitted with a Tokina 100 mm lens. The CMOS sensor, which has a resolution of 1024 × 1024 pixels each with a size of 20 μm × 20 μm, was cropped to 640 × 1024 pixels resulting in a field of view of 56 × 88 mm. The investigated flame was imaged using high-speed PIV recordings. The high-speed recordings were taken to obtain time-averaged statistics of the reacting flow field and to capture flame–flow interaction. For the recordings the frame rate was set to 4.5 kHz and a total of 5000 image pairs were collected. A relatively short recording time minimizes the buildup of seeding particles on the glass walls, resulting in improved flame front detection.

A LaVision programmable timing unit was used to synchronize the laser pulses and the high-speed camera. The time interval between two consecutive pulses of the laser was set to 40 μs, resulting in an average particle displacement of around 8–15 pixels between two consecutive images within an image pair. Both the acquisition and processing of the PIV images were done with Davis 10.2 (LaVision). A multi-pass cross-correlation approach, one pass with an interrogation window of 48 × 48 pixels and three passes with an interrogation window of 24 × 24 pixels, was used. All interrogation windows have an overlap of 50%. Post-processing of the velocity vectors is done by means of a median filter with universal outlier detection to remove spurious vectors.

2.3. Flame configuration

Fig. 3 illustrates the possible positions and shapes of the flame within the combustor. Since it appeared difficult to record a premixed pure hydrogen flame with a consumer camera (Nikon D5600), a flame with $\phi = 0.4$, H_2%=80 at $Re = 11.61 \times 10^3$ was used. The flames considered in this study (listed in Table 1) have an almost identical flame position and shape to the flame shown in Fig. 3. Additionally, this figure shows three potential flame positions: flashback position (green line), actual position (red line) and downstream position (orange line). In this study, the flames are located along the red line for both cases (R-1 and R-2). For clarity, the flashback location indicated by the green line in Fig. 3 represents an undesired upstream flame stabilization within the trapped-vortex combustor. It does not correspond to a complete flashback through the main-flow inlet channel, which would only occur if the main-flow inlet velocity were further reduced. This topic will be discussed in more detail in Section 4.2.5. Furthermore, it can be seen that the flame is attached to the tip of the inner liner.

3. Methodology

Understanding the interaction between the flame and flow requires detailed information about both the instantaneous and time-averaged location of the flame front and the corresponding flow fields. To achieve this, Favre-averaged quantities were derived from PIV data, as described in Section 3.1. The methodology for detecting both the instantaneous and average flame front is described in Section 3.2.

3.1. Favre-averaged quantities from PIV data

In standard PIV the mean of a velocity component in a particular interrogation area is determined from the arithmetic mean of all instantaneous velocities, resulting in a Reynolds-averaged velocity component. In combustion studies, however, it is often more relevant to consider Favre-averaged (density-weighted) quantities, which require information on both the instantaneous velocity and the instantaneous gas density in that interrogation area. The latter is not directly available from PIV, but procedures are available to estimate the instantaneous gas density from PIV measurements [8,9]. One procedure, that is applicable to premixed adiabatic flames, relies on an accurate determination of the flame front in each instantaneous PIV image, resulting in a bimodal density distribution, i.e. a clear distinction between the unburnt (reactants) and burnt (products) regions [8], which has been discussed in a previous study by Altenburg et al. [9]. However, in the flames investigated in the present study, the recirculation and mixing of hot products into the fresh reactants may violate this bimodal assumption, making it difficult to clearly distinguish the unburnt and burnt regions. Therefore, in this study another procedure is employed, in which it is assumed that the instantaneous number of seeding particles in an interrogation area is (on average) proportional to the local gas density. This is reasonable as long as the particles do not burn or evaporate in the flame. The number of seeding particles is taken to be proportional to the sum of the pixel intensities in the interrogation area. The differences between these two procedures have been discussed in detail in a previous study involving premixed jet flames, see Altenburg et al. [9].

3.2. Flame front detection method

The histogram-based method described in Altenburg et al. [9] is used to determine the instantaneous flame front in each instantaneous PIV image. In this method a flame front in an instantaneous PIV image was identified from the change of the local particle number density using a bilateral filter, i.e. utilizing both spatial and intensity information of a raw Mie-scattering image. The bilateral filter applies a weighting function, consisting of a spatial and an intensity Gaussian kernel, to each pixel in the image. The diameter of each pixel neighbourhood, that is used during filtering, was set to 11 pixels, which corresponds to a physical distance of 1 mm. The spatial standard deviation, which characterizes the spatial kernel, was set to $2\sqrt{2\ln(2)}$, resulting in a spatial kernel that has a full-width-at-half-maximum equal to the neighbourhood diameter. The intensity standard deviation, which characterizes the intensity kernel, was set to 0.1, corresponding to 10% of the maximum intensity range of the image. Due to the unavoidable presence of laser-light reflections, a pre-processing step is conducted to improve the accuracy of the flame front detection. This pre-processing step involves subtracting the minimum intensity observed over a symmetric time window of 99 images centered around the reference time. This correction is applied to account for the gradual buildup of seeding particles on the U-bend wall during the measurement run. Accurate flame front detection was achieved using the pre-processing step and the chosen bilateral filter settings, as shown in Fig. 4 for the premixed hydrogen–air flame studied (case R-2). The time-averaged flame front was determined by applying the aforementioned method to the averaged image obtained from the pre-processed images.

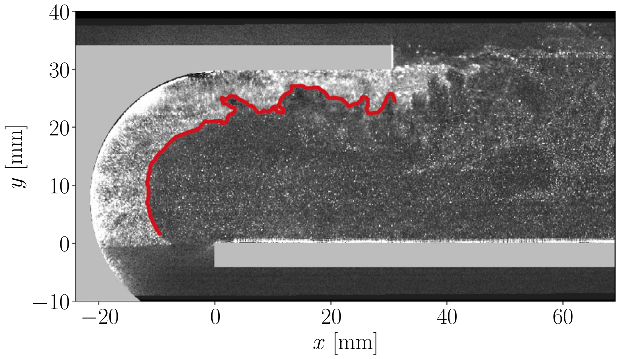

Fig. 4. A pre-processed instantaneous image (case R-2), i.e. subtracting the minimum intensity observed over a moving time interval with a width of 99 images, centered around the reference raw Mie-scattering image. The red line indicates the detected instantaneous flame front.

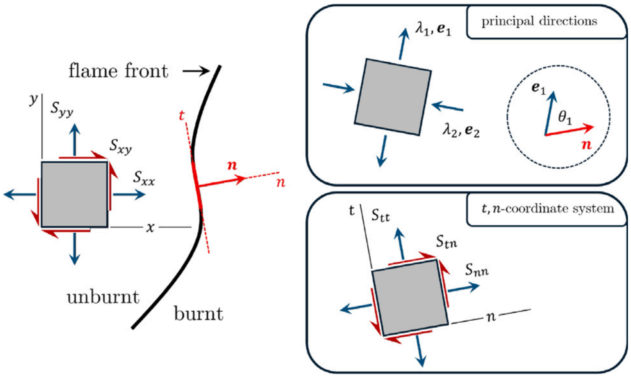

Fig. 5. Illustration of the orientation between the flame front normal $\mathbf{n}$ and the principal strain rate directions $\mathbf{e}_1$ (most extensive) and $\mathbf{e}_2$ (most compressive). The two-dimensional strain rate tensor $\mathbf{S}$ can be characterized by its principal eigenvalues (eigenvectors) λ_1 ($\mathbf{e}_1$) and λ_2 ($\mathbf{e}_2$). The angle θ_1 is the angle between the most extensive strain rate $\mathbf{e}_1$ and the flame front normal $\mathbf{n}$. $\mathbf{S}$ in the Cartesian x, y-coordinate system can also be transformed to the curvilinear t, n-coordinate system, which is tangential and normal to the local flame front.

3.3. Analysis of the strain rate tensor and flame front alignment

Fig. 5 illustrates the orientation between the flame front normal vector $\mathbf{n}$ and the principal strain rate directions $\mathbf{e}_1$ and $\mathbf{e}_2$. These principal directions correspond to the most extensive and compressive strain rates, respectively, of the two-dimensional strain rate tensor $\mathbf{S}$ in the Cartesian x, y-coordinate system. The two-dimensional strain rate tensor is defined as:

$$\mathbf{S} = \begin{bmatrix} S_{xx} & S_{xy} \\ S_{yx} & S_{yy} \end{bmatrix} = \begin{bmatrix} \dfrac{\partial u_x}{\partial x} & \dfrac{1}{2}\left(\dfrac{\partial u_x}{\partial y} + \dfrac{\partial u_y}{\partial x}\right) \\ \dfrac{1}{2}\left(\dfrac{\partial u_x}{\partial y} + \dfrac{\partial u_y}{\partial x}\right) & \dfrac{\partial u_y}{\partial y} \end{bmatrix}, \tag{1}$$

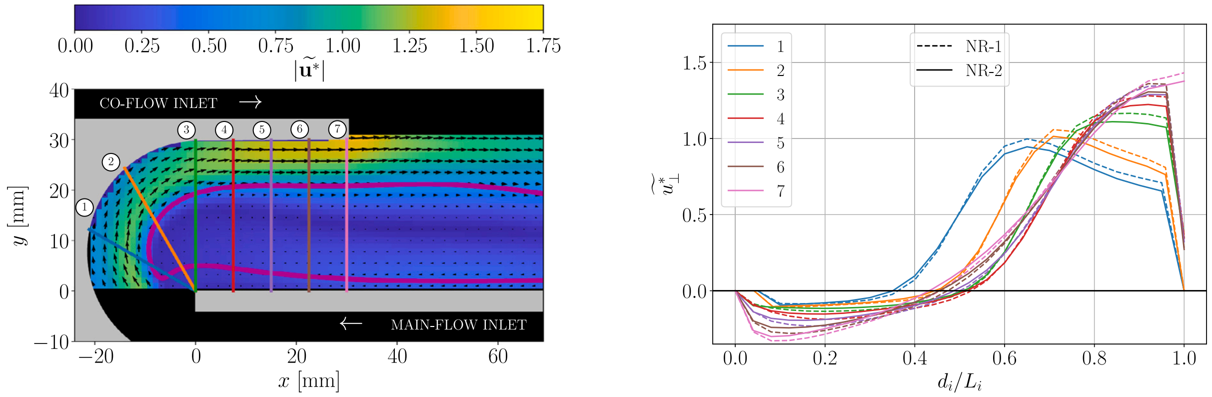

(a)

(b)

Fig. 6. (a) The Favre-averaged velocity vectors $\widetilde{\mathbf{u}}$ for case NR-2. The background color corresponds to the dimensionless velocity magnitude $|\widetilde{\mathbf{u}^*}| = |\widetilde{\mathbf{u}}|/U_b$. (b) The extracted dimensionless velocity profiles of the velocity component perpendicular ($\widetilde{u_\perp^*}$) to the lines shown in Fig. 6(a) for case NR-1 (dashed lines) and case NR-2 (solid lines). The magenta line indicates the boundary of the recirculation zone.

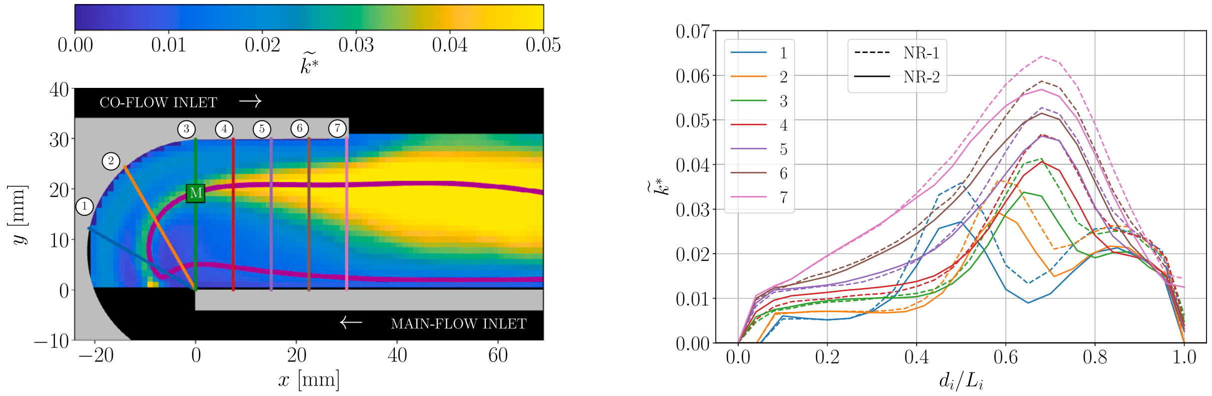

(a)

(b)

Fig. 7. (a) The dimensionless Favre-averaged turbulent kinetic energy field $\widetilde{k}^* = \widetilde{k}/U_b^2$ for case NR-2. The green 'M' marks the location of a monitoring point. (b) The extracted profiles of $\widetilde{k}^*$ along the lines (1–7) shown in Fig. 7(a) for case NR-1 (dashed lines) and case NR-2 (solid lines).

where u_x and u_y are the x- and y-velocity components, respectively (see Fig. 5). In this formulation, $\mathbf{S}$ is symmetric, so that $S_{xy} = S_{yx}$.

The two-dimensional strain rate tensor $\mathbf{S}$ is characterized by its principal eigenvalues, λ_1 and λ_2, and the corresponding eigenvectors, $\mathbf{e}_1$ and $\mathbf{e}_2$, with $\lambda_1 \geq \lambda_2$. The eigenvalues and eigenvectors are interpolated to the average flame front location (red dashed line) in Fig. 10. By convention, λ_1 corresponds to the most extensive strain rate, while λ_2 represents the most compressive strain rate of the flow, with eigenvectors $\mathbf{e}_1$ and $\mathbf{e}_2$ indicating their respective directions. In this study, the alignment of the flame front and the principal strain rate directions is characterized by the angle θ_1, which is the angle between the normal of the average flame front location $\mathbf{n}$ and the eigenvector $\mathbf{e}_1$, i.e. the direction of the most extensive principal strain rate. In this study, the fixed Cartesian x, y-coordinate system is not always suitable for comparing flow-field profiles. Therefore, a curvilinear t, n-coordinate system, with axes tangential and normal to the local flame front, is sometimes used. Fig. 5 visualizes the transformation of the two-dimensional strain rate tensor $\mathbf{S}$ in the Cartesian x, y-coordinate system to the curvilinear t, n-coordinate system.

4. Results

4.1. Non-reacting flow field

Fig. 6(a) shows the Favre-averaged velocity vectors $\widetilde{\mathbf{u}}$ for case NR-2 ($Re = 13.55 \times 10^3$). The background color represents the dimensionless velocity magnitude $|\widetilde{\mathbf{u}^*}| = |\widetilde{\mathbf{u}}|/U_b$. The flow field has a trapped vortex (recirculation zone) adjacent to the inner liner and a thick region of low velocity near the U-bend wall. High velocities are observed near the wall at the U-bend extension. This figure is qualitatively very similar to that of case NR-1 ($Re = 9.68 \times 10^3$), which is not shown here for brevity. For the non-reacting cases, Reynolds and Favre averaging yield nearly identical results, which were verified but are not presented here.

Fig. 6(b) provides a more quantitative comparison of the velocity profiles between the two cases (case NR-1: dashed lines, case NR-2: solid lines). It shows the profiles of the dimensionless velocity component perpendicular ($\widetilde{u_\perp^*} = \widetilde{u_\perp}/U_b$) to the (colored) lines in Fig. 2. These lines are given by $d_i(x, y)$ and are normalized with their corresponding length L_i with $i = 1, 2, \ldots, 7$. The lines span from the inner liner (tip), where $d_i/L_i = 0$, to the U-bend (extension) wall, where $d_i/L_i = 1$. It can be seen that case R-1 (the lower Reynolds number) exhibits a slightly higher value of $\widetilde{u_\perp^*}$ close to the wall of the U-bend (extension).

To compare the inlet bulk velocity measured by the mass flow controllers ($U_{b,\mathrm{MFC}}$) with that derived from PIV measurements, the velocity profiles were integrated from the coordinate starting at the inner liner tip ($d_i/L_i = 0$), to the coordinate at the U-bend (extension) wall ($d_i/L_i = 1$). These resulting integrated values were then divided by the inlet height h_1 to obtain a bulk velocity from the PIV data $U_{b,\mathrm{PIV}}$. These values were compared to $U_{b,\mathrm{MFC}}$, with an average deviation of approximately −4.3% and −5.2% for case NR-1 and NR-2, respectively. A possible source of this deviation is the non-zero velocities at the walls in the velocity profiles, which can be attributed to limitations of the PIV

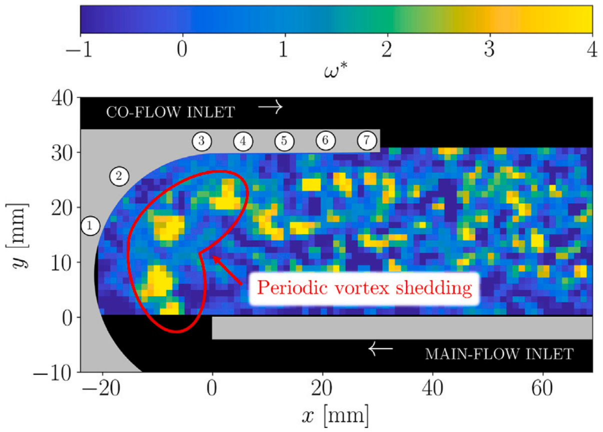

Fig. 8. The instantaneous dimensionless vorticity $\omega^* = \omega h_1/U_b$ for case NR-1.

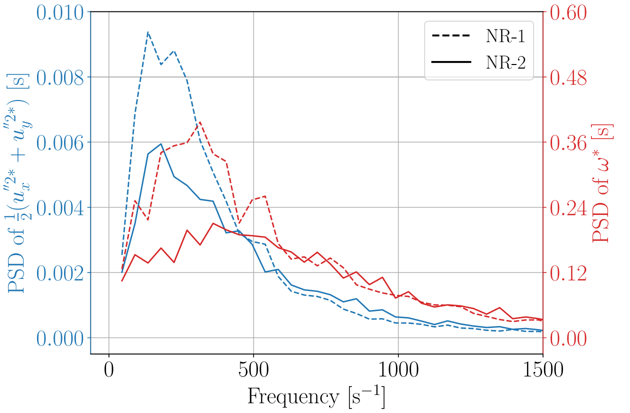

Fig. 9. Power spectral density of the instantaneous dimensionless turbulent kinetic energy (blue lines) and the instantaneous vorticity (red lines) obtained at the monitoring point marked ‘M’ in Fig. 7(a), for both cases NR-1 and NR-2.

system to resolve near-wall velocities, due to reflections and the finite size of the interrogation windows. Furthermore, the red (4), purple (5) and brown (6) lines in Fig. 6(b) display steep velocity gradients near the wall in the U-bend extension. The figure also shows a long recirculation zone, indicated by the magenta line, which extends beyond the field of view of the PIV system.

Fig. 7(a) shows the dimensionless Favre-averaged turbulent kinetic energy field $\widetilde{k^*} = \widetilde{k}/U_b^2$, where $\widetilde{k} = \frac{1}{2}(\widetilde{u_x^{\prime\prime 2}} + \widetilde{u_y^{\prime\prime 2}})$, for case NR-2. The figure indicates a region with increased turbulent kinetic energy at the boundary of the recirculation zone, which could be attributed to vortex shedding occurring in the strong shear layer. In this region, which corresponds to the first peak of the blue (1), orange (2) and green (3) lines in Fig. 7(b), it can be seen that case NR-1 has larger dimensionless turbulent kinetic energy compared to case NR-2. This can be explained by the difference in vortex shedding between the two cases. Fig. 8 illustrates the periodic vortex shedding originating from the blunt liner tip. It shows a snapshot of the instantaneous dimensionless vorticity $\omega^* = \omega h_1/U_b$ for case NR-1. The instantaneous vorticity ω was determined as:

$$\omega = \frac{\partial u_y}{\partial x} - \frac{\partial u_x}{\partial y}. \tag{2}$$

Application of the Q-criterion [10] (not shown for brevity) confirmed that the isolated pockets with high vorticity were individual vortices. To investigate the vortex shedding, a monitoring point, labelled ‘M’, was placed at the maximum of $\widetilde{k^*}$ along the green line (line 3) in Fig. 7(a). A fast Fourier transform analysis was performed on the signal of the instantaneous dimensionless vorticity ω^* and the instantaneous dimensionless turbulent kinetic energy, defined as $\frac{1}{2}(u_x^{\prime\prime 2*} + u_y^{\prime\prime 2*})$. The power spectral density (PSD) of these signals was then extracted. Fig. 9 presents the resulting PSDs for the instantaneous dimensionless turbulent kinetic energy (blue lines) and the instantaneous dimensionless vorticity (red lines). It can be observed that case NR-1 exhibits a significantly higher peak value for ω^* (red dashed line) compared to case NR-2 (red solid line). Furthermore, the PSD of ω^* also indicates that its power is more concentrated at lower frequencies for case NR-1 than for case NR-2. Examining the PSD of the instantaneous dimensionless turbulent kinetic energy $\frac{1}{2}(u_x^{\prime\prime 2*} + u_y^{\prime\prime 2*})$, again a significantly higher value is observed for case NR-1 compared to NR-2. Physically, these results suggest the following: case NR-1, characterized by the lower Reynolds number, exhibits vortex shedding at a lower frequency than case NR-2. However, the vortical structures in case NR-1 contain more dimensionless kinetic energy compared to case NR-2.

Another interesting observation in Fig. 7(a) is the region with high $\widetilde{k^*}$ close to the wall in the U-bend. This can be observed in more detail in Fig. 7(b), where the profiles of $\widetilde{k^*}$ in the U-bend (blue (1), orange (2) and green (3) lines) show an increase when approaching the U-bend wall ($d_i/L_i \gtrapprox 0.7$). In this region, also, a higher value of $\widetilde{k^*}$ is observed for case NR-1 compared to NR-2. Note that the relatively high values of $\widetilde{k^*}$ close to the U-bend wall match the relatively thick boundary layer on the U-bend wall in Fig. 6(a). It is speculated that this is linked to a secondary flow pattern in the form of Görtler-type vortices that may appear in boundary layers flowing along concave walls [11–13]. Unfortunately, this hypothesis could not be tested, as no velocity data in the span-wise direction is available in the present experiment.

4.2. Reacting flow field

4.2.1. The location of the flame front

Fig. 10 presents the probability density of the instantaneous flame fronts, as determined by the method outlined in Section 3.2, for case R-1 and R-2. In both cases, a concentrated distribution is observed in the U-bend, indicating a steady, laminar-like flame front in this region. Further downstream, the distribution becomes more diffuse, indicating a more intermittent flame front behaviour. This is more pronounced in case R-1 (marginally stable flame), where the flame front exhibits greater fluctuations, compared to case R-2 (highly stable flame), where the flame front distribution remains more concentrated. For a qualitative view of the flame front, we refer to Fig. 4, which illustrates an instantaneous snapshot of the flame front for case R-2: a steady, laminar-like front within the U-bend with a more wrinkled flame front downstream. A fixed Cartesian reference axis is not suitable for comparing flow-field profiles due to the U-bend. Therefore, the average location of the flame front (red dashed line in Fig. 10), which closely follows the U-bend’s curvature, was chosen as the reference axis throughout this study. The two cases R-1 (see Fig. 10(a)) and R-2 (see Fig. 10(b)) show an almost identical average flame front location. To be more precise, the part of the red curve between the two spherical markers is used as the reference axis, denoted as $c_f(x, y)$, with its corresponding length indicated by L_f. This reference axis c_f is used throughout this section to extract the turbulent kinetic energy (Section 4.2.3), the strain rate tensors (Section 4.2.4) and the velocity profiles (Section 4.2.5). The starting point (the red spherical marker at $y = 3.0$ mm) was chosen to maintain sufficient distance from the boundaries of the field of view of the PIV system, where the performance of PIV tends to degrade. The end point of c_f (the red spherical marker at $x = 17.5$ mm) corresponds to the location where the average flame front location of case R-1 starts to deviate from that of case R-2.

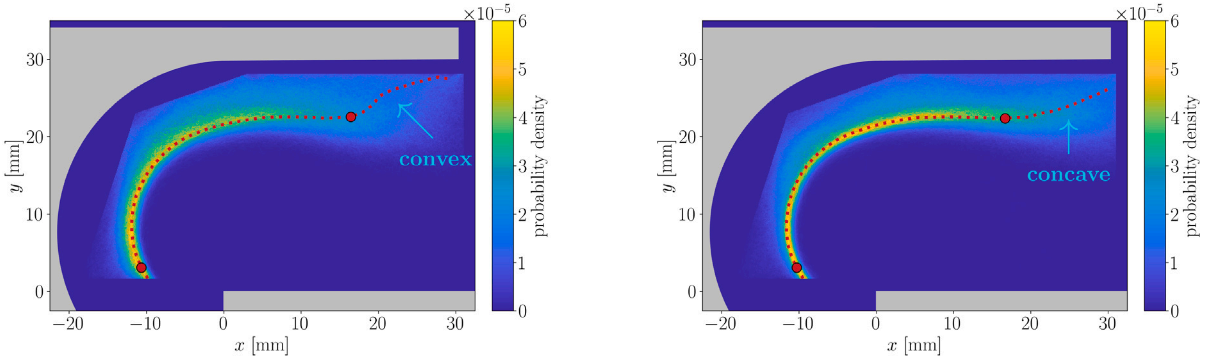

(a) case R-1

(b) case R-2

Fig. 10. The probability density of the instantaneous flame fronts for cases R-1 and R-2. The red dotted curve indicates the average flame front location that was determined using the method described in Section 3.2. The part of the red curve between the two spherical markers, denoted as curve $c_f(x, y)$ (with length L_f), serves as reference axis throughout the remainder of this study. At the downstream end of the U-bend, the average flame front is convex towards the unburnt region for case R-1, whereas it is concave for case R-2.

4.2.2. *The velocity field*

Figs. 11(a) and 12(a) show the Favre-averaged velocity vectors and the dimensionless velocity magnitude $|\widetilde{\mathbf{u}^*}| = |\widetilde{\mathbf{u}}|/U_b$ for cases R-1 and R-2, respectively. It can be seen that both cases show recirculation zones of similar size, with the recirculation zone of R-1 being slightly more compact compared to R-2. By comparing the velocity profiles for R-1 and R-2 (in Figs. 11(b) and 12(b)), it can be seen that the profiles are similar throughout the U-bend (blue (1), orange (2) and green (3) lines). However, further downstream, at the end of the U-bend extension, the velocity profiles for R-1 are elevated compared to those for R-2. This observation can be attributed to the local orientation of the average flame front in this region, as seen in Fig. 10. The figure shows that the flame front in this region is convex towards the unburnt region for case R-1, whereas it is concave for case R-2. As a result, the angle between the flame front and the positive y-axis is smaller in R-1 than in R-2. This leads to an increased velocity ratio across the flame front in R-1, resulting in a higher value of $|\widetilde{\mathbf{u}^*}|$. This is consistent with the behaviour observed in premixed unconfined jet flames [9].

Fig. 13 shows the tangential ($\widetilde{u_t^*}$) and normal ($\widetilde{u_n^*}$) components of the dimensionless Favre-averaged velocity extracted along the average flame front location (red curves in Figs. 11(a) and 12(a)) for both cases R-1 and R-2. It is clear that the normal velocity component is nearly zero within the U-bend ($c_f/L_f \lessapprox 0.5$), so the flow is primarily tangential to the average flame front location, indicating no expansion across the average flame front.

4.2.3. *The turbulent kinetic energy field*

Figs. 14(a) and 15(a) show the dimensionless Favre-averaged turbulent kinetic energy field $\widetilde{k^*} = \widetilde{k}/U_b^2$ for cases R-1 and R-2, respectively. Similarly to the non-reacting flows, a region of elevated $\widetilde{k^*}$ is observed close to the U-bend wall ($d_i/L_i \gtrapprox 0.7$ for the blue (1), orange (2) and green (3) lines). The higher values of $\widetilde{k^*}$ are slightly more pronounced for R-1 compared to R-2, as shown in more detail in Figs. 14(b) and 15(b). Another observation is the suppression of the turbulent kinetic energy at the boundary of the recirculation zone in the U-bend, whereas this is a region of increased turbulent kinetic energy due to vortex shedding for the non-reacting flows. Furthermore, as shown in Figs. 14(a) and 15(a), the average flame front (red curve) is located in a region where $\widetilde{k^*}$ has a minimum. This is also illustrated by the triangular markers in Figs. 14(b) and 15(b), which indicate the average location of the flame front. In Fig. 16 the dimensionless turbulent kinetic energy profile, $\widetilde{k^*}$, along the average location of the flame front, shows a clear difference between the two cases. Case R-1, operating under marginally stable flame conditions, exhibits significantly higher values along the entire profile compared to case R-2, which corresponds to a highly stable flame. Within the U-bend ($c_f/L_f \lessapprox 0.5$), this increase can be attributed to the greater dimensionless shear strain, which could be likely linked to the difference in vortex shedding that was observed for the corresponding non-reacting cases NR-1 and NR-2.

The two-dimensional dimensionless strain rate tensor of the Favre-averaged flow, $\widetilde{\mathbf{S}^*}$, was first determined in the Cartesian x, y-coordinate system and subsequently transformed to the curvilinear t, n-coordinate system that is aligned with the average flame front location (reference axis: curve c_f). Fig. 17 shows the three resulting components of $\widetilde{\mathbf{S}^*}$: tangential, normal and shear strain rate. Here, the subscripts 't' and 'n' refer to directions tangential and normal to the average flame front. These components have been made dimensionless by multiplication with a fixed length scale h_1 (the height of the main-flow inlet) and division by its corresponding bulk velocity U_b, so that $\widetilde{\mathbf{S}^*} = \widetilde{\mathbf{S}} h_1/U_b$, where the strain rate tensor of the Favre-averaged flow $\widetilde{\mathbf{S}}$ is defined as:

$$\widetilde{\mathbf{S}} = \begin{bmatrix} \widetilde{S_{tt}} & \widetilde{S_{tn}} \\ \widetilde{S_{nt}} & \widetilde{S_{nn}} \end{bmatrix} = \begin{bmatrix} \dfrac{\partial \widetilde{u_t}}{\partial t} & \dfrac{1}{2}\left(\dfrac{\partial \widetilde{u_t}}{\partial n} + \dfrac{\partial \widetilde{u_n}}{\partial t}\right) \\ \dfrac{1}{2}\left(\dfrac{\partial \widetilde{u_t}}{\partial n} + \dfrac{\partial \widetilde{u_n}}{\partial t}\right) & \dfrac{\partial \widetilde{u_n}}{\partial n} \end{bmatrix}, \tag{3}$$

where $\widetilde{u_t}$ and $\widetilde{u_n}$ are the t- and n-components of the Favre-averaged velocity, i.e. the tangential and normal velocity components along the reference axis c_f (see Fig. 10). The figure shows that a greater dimensionless shear strain $\widetilde{S_{tn}^*}$ within the U-bend can be observed in case R-1 compared to R-2. In regions of strong shear (case R-1), the steep velocity gradients result in elevated turbulent kinetic energy. This increased dimensionless shear leads to stronger dimensionless turbulent kinetic energy compared to regions with weaker dimensionless shear (case R-2).

In both cases, a strong shear layer within the U-bend is observed, with $\widetilde{S_{tn}^*}$ as the dominant component of $\widetilde{\mathbf{S}^*}$. Downstream of the U-bend ($c_f/L_f \gtrapprox 0.5$) the shear layer weakens. The higher values of the dimensionless turbulent kinetic energy profile $\widetilde{k^*}$ in R-1 compared to R-2 in this region could be attributed to increased intermittency of the flame front in R-1. This is supported by Fig. 10, which shows that the flame front distribution becomes more diffuse downstream for R-1 compared to R-2, indicating a more intermittent flame front for R-1. Furthermore, the non-zero value for the normal strain rate $\widetilde{S_{nn}^*}$, indicates the expansion induced by combustion, which reaches a minimum at $c_f/L_f \approx 0.43$ for both cases. Another interesting observation from Fig. 17 is the low value of the tangential strain rate $\widetilde{S_{tt}^*}$. From the definition of flame straining, the strain rate at the flame front, particularly the tangential strain rate $\widetilde{S_{tt}^*}$ affects the flame surface area and thus the flame speed [14].

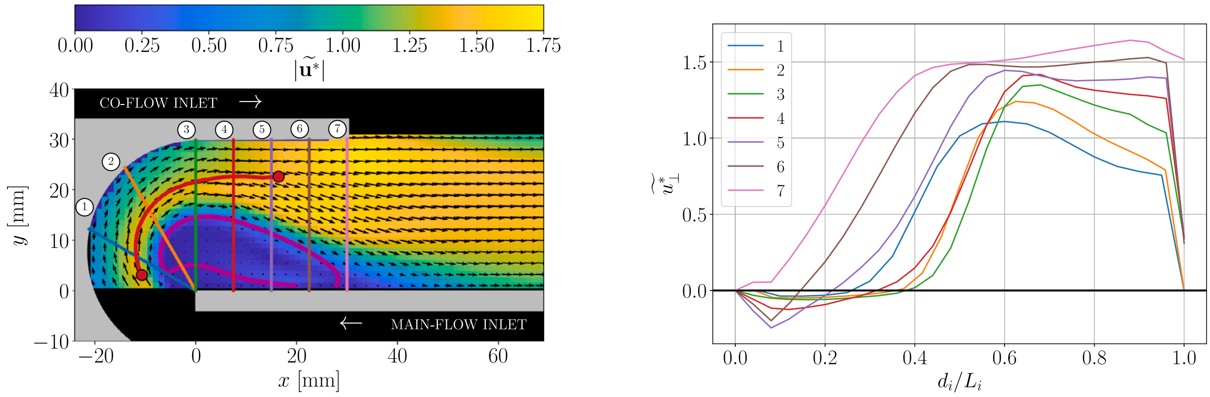

(a)

(b)

Fig. 11. (a) The Favre-averaged velocity vectors $\widetilde{\mathbf{u}^*}$ for case R-1. The background color corresponds to the dimensionless velocity magnitude $|\widetilde{\mathbf{u}^*}| = |\widetilde{\mathbf{u}}|/U_b$. (b) The extracted dimensionless velocity profiles of the velocity component perpendicular ($\widetilde{u^*_\perp}$) to the lines shown in Fig. 11(a). The red curve indicates the average flame front location (as shown in Fig. 10(a)) and the magenta line indicates the boundary of the recirculation zone.

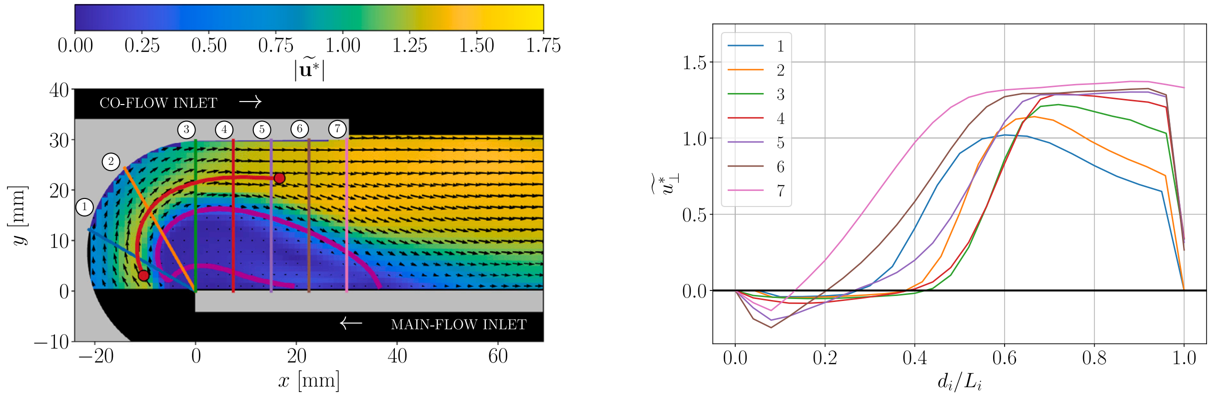

(a)

(b)

Fig. 12. (a) The Favre-averaged velocity vectors $\widetilde{\mathbf{u}}$ for case R-2. The background color corresponds to the dimensionless velocity magnitude $|\widetilde{\mathbf{u}^*}| = |\widetilde{\mathbf{u}}|/U_b$. (b) The extracted dimensionless velocity profiles of the velocity component perpendicular ($\widetilde{u^*_\perp}$) to the lines shown in Fig. 12(a). The red curve indicates the average flame front location (as shown in Fig. 10(b)) and the magenta line indicates the boundary of the recirculation zone.

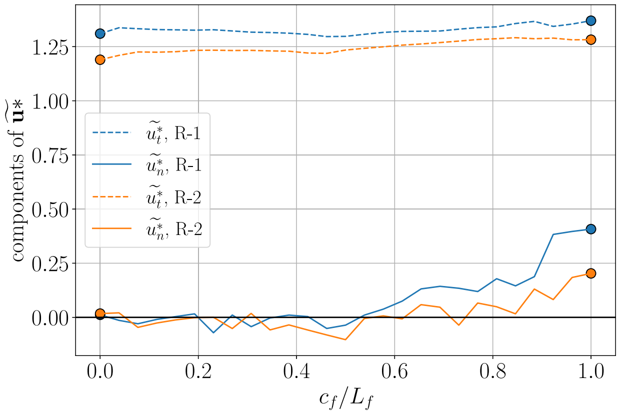

Fig. 13. Profiles of the tangential ($\widetilde{u^*_t}$) and normal ($\widetilde{u^*_n}$) components of the dimensionless Favre-averaged velocity extracted along the average flame front location (red curves in Figs. 11(a) and 12(a)) for cases R-1 and R-2. Since the normal velocity component is nearly zero within the U-bend ($c_f/L_f \leq 0.5$), the flow is almost entirely tangential to the average flame front, indicating no expansion across the average flame front.

4.2.4. Alignment of flame front and the principal strain rates

In relation to the laminar-like behaviour of the flame front within the U-bend, an analysis was conducted similar to previous numerical and experimental studies [15–23], to quantitatively examine the alignment between the strain rate and the orientation of the flame front. The discrepancies in the degree of alignment between strain rates and the flame front observed across these studies indicate that factors such as flame configuration, definition of the flame front location, turbulence intensity and combustion regimes (characterized by Karlovitz number Ka and Damköhler number Da) can significantly influence this behaviour. In the present study, the two reacting cases R-1 and R-2 are characterized by $Ka = 43$ ($Da = 0.13$) and $Ka = 66$ ($Da = 0.10$), respectively. The determination of these values is provided in the Appendix.

Fig. 18 shows the angle θ_1 (defined in Fig. 5) along the average flame front location (labelled: 0 mm) and two distances perpendicular to the average flame front location on the unburnt side (labelled: 1 mm and 2 mm). These two additional distances were considered to see whether the results regarding the alignment between the strain rate and the flame front vary strongly with increasing distance from the average flame front location. The black dashed line indicates an angle $\theta_1 = 45°$, which serves as a reference to indicate pure shear straining, which means that $\widetilde{S^*_{tn}}$ is the dominant component of $\widetilde{\mathbf{S}^*}$. A value $\theta_1 = 0°$ would indicate that the normal of the average flame front location and the most extensive principal strain rate are perfectly aligned.

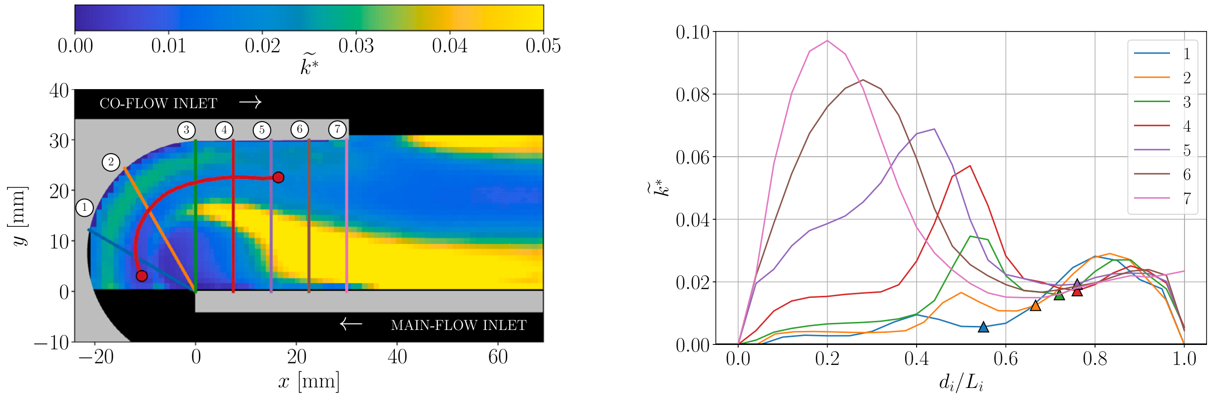

(a) (b)

Fig. 14. (a) The dimensionless Favre-averaged turbulent kinetic energy field $\widetilde{k}^* = \widetilde{k}/U_b^2$ for case R-1, where the red curve indicates the average location of the flame front, which is situated between regions with higher turbulent kinetic energy $\widetilde{k}^*$. (b) The extracted profiles of $\widetilde{k}^*$ along the lines (1–7) shown in Fig. 14(a), where the triangular markers indicate the average location of the flame front.

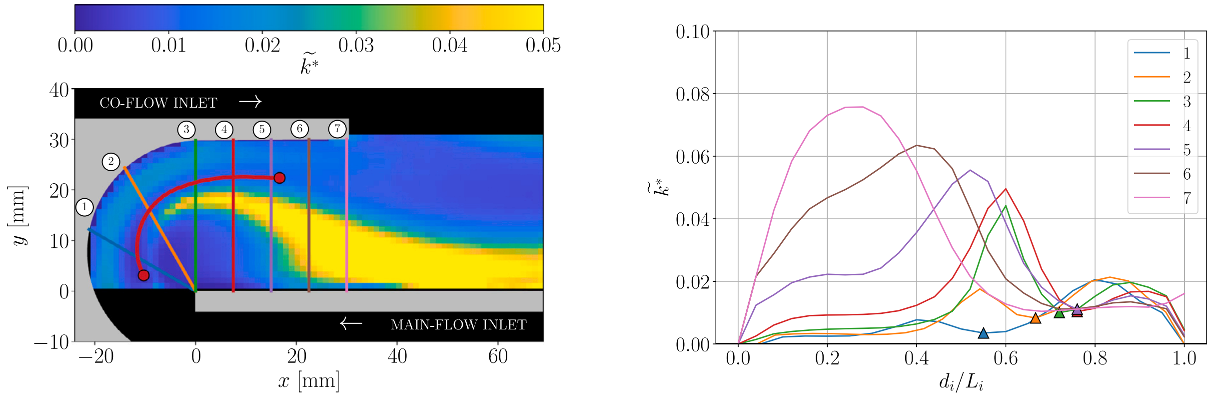

(a) (b)

Fig. 15. (a) The dimensionless Favre-averaged turbulent kinetic energy field $\widetilde{k}^* = \widetilde{k}/U_b^2$ for case R-2, where the red curve indicates the average location of the flame front. The average location of the flame front is situated at a position between regions with higher turbulent kinetic energy $\widetilde{k}^*$. (b) The extracted profiles of $\widetilde{k}^*$ along the lines (1–7) shown in Fig. 15(a), where the triangular markers indicate the average location of the flame front.

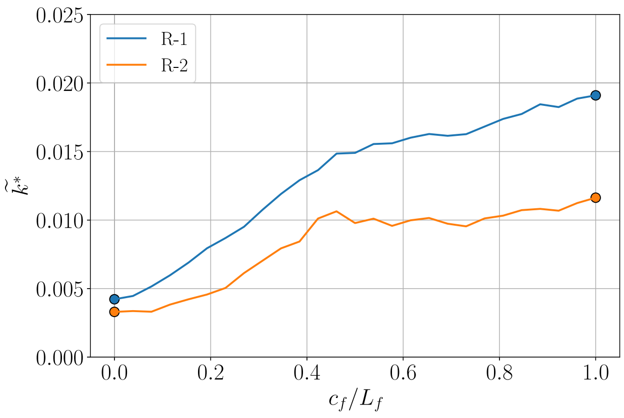

Fig. 16. Profiles of the dimensionless Favre-averaged turbulent kinetic energy $\widetilde{k}^*$ extracted along the average location of the flame front (red curve in Fig. 15(a)) for both cases R-1 and R-2. Case R-1 (the lower Reynolds number) shows higher values along the entire profile, attributed to the relative stronger shear layer (within the U-bend, $c_f/L_f \lessapprox 0.5$) and to the greater flame front intermittency (downstream of the U-bend, $(c_f/L_f \gtrapprox 0.5)$.

Within the U-bend $(c_f/L_f \lessapprox 0.5)$, the values of θ_1 along the average flame front location (0 mm) start at approximately 25° for case R-1 and 10° for case R-2. These values increase to 45°, which illustrates the combined effect of the shear strain $\widetilde{S}^*_{tn}$ and the combustion-induced expansion $\widetilde{S}^*_{nn}$ on the alignment. This effect is clearly illustrated in Fig. 17(b). At the start of the average flame front location, $\widetilde{S}^*_{nn}$ dominates over $\widetilde{S}^*_{tn}$, causing the average flame front normal to align with the most extensive strain (see Fig. 18). Further along the curve, $\widetilde{S}^*_{nn}$ decreases while $\widetilde{S}^*_{tn}$ increases towards an angle $\theta_1 = 45°$, which indicates a region of strong shear straining. With increasing distance from the average flame front location (1 mm and 2 mm), the values for θ_1 remain consistently close to 45° within the U-bend. This indicates an absence of $\widetilde{S}^*_{nn}$ and a dominance of the shear strain component $\widetilde{S}^*_{tn}$ in this region. This result holds for both cases and is in agreement with the findings of Wang et al. [20], who observed the same value at the base of a high Karlovitz $(Ka = 253)$ premixed methane–air jet flame. In this region, the influence of turbulence on the flame geometry is minimal, allowing the flame front to have a laminar-like structure. The 45° alignment of the average flame front normal and the principal eigenvectors $\mathbf{e}_i$ in the upstream region $(c_f/L_f \lessapprox 0.5)$ lacks a clear explanation but may indicate a universal connection to shear-dominated mechanisms.

Downstream of the U-bend $((c_f/L_f \gtrapprox 0.5)$, the average flame front normal $\mathbf{n}$ increasingly aligns with the direction of the most extensive strain rate $\mathbf{e}_1$, which is in agreement with (recent) numerical studies [15,16,21–23] and experimental results [18,19]. This can be

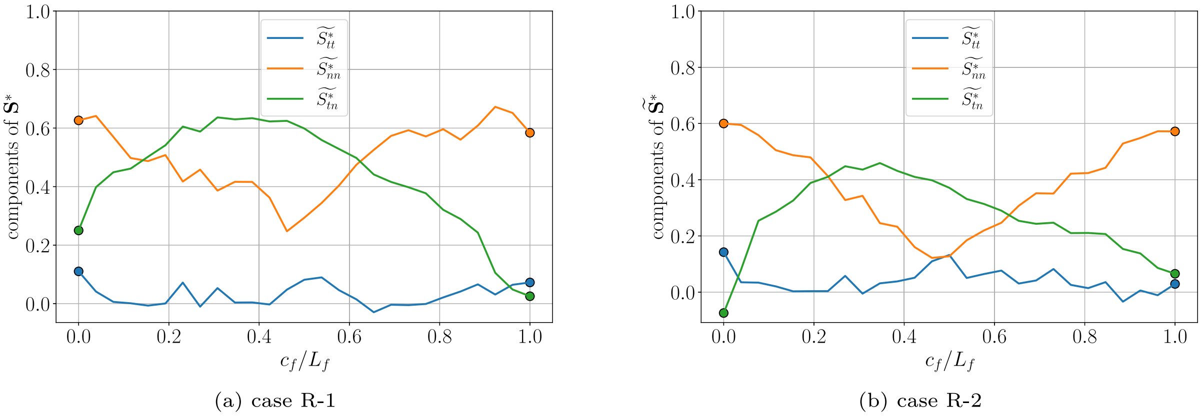

(a) case R-1

(b) case R-2

Fig. 17. (a) The dimensionless strain rate profiles $\widetilde{S_{tt}^*}$, $\widetilde{S_{nn}^*}$ and $\widetilde{S_{tn}^*}$ for case R-1 and case R-2, extracted along the average flame front location.

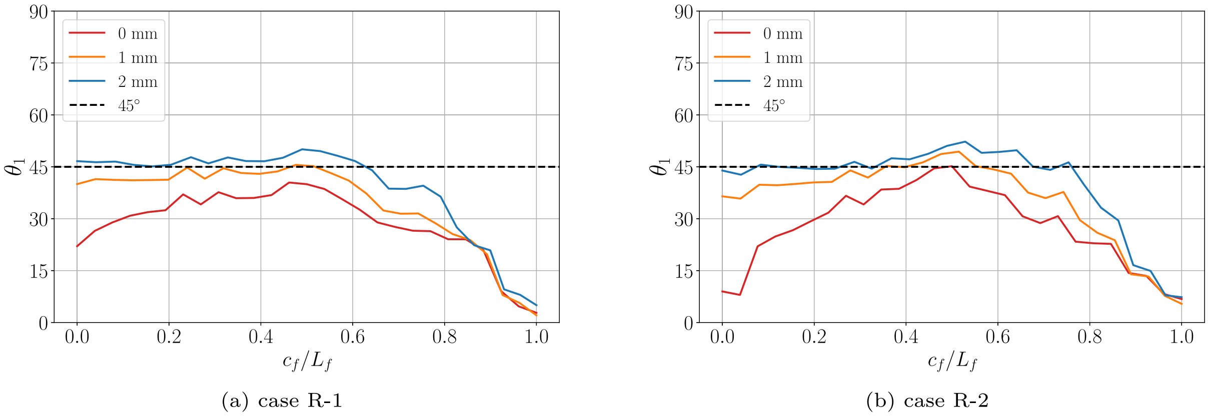

(a) case R-1

(b) case R-2

Fig. 18. The angle θ_1 along the average flame front location (labelled: 0 mm) and two distances perpendicular to the average flame front location on the unburnt side (labelled: 1 mm and 2 mm). The angle θ_1 is the angle between the normal of the average flame front location **n** and the eigenvector $\mathbf{e}_1$, i.e. the direction of the most extensive principal strain rate, for case R-1 and case R-2. The black dashed line represents an angle of 45° and is used as a reference to indicate pure shear straining. A value $\theta_1 = 0°$ indicates that the normal of the average flame front location and the most extensive principal strain rate are perfectly aligned.

attributed to the increase in the combustion-induced expansion $\widetilde{S_{nn}^*}$ (see Fig. 17) that accelerates the flow in the average flame front normal direction resulting in extensive strain rates in this direction. This means that this region can be regarded as a weakly turbulent flame, where the expansion strain rate $\widetilde{S_{nn}^*}$ within the flame dominates over turbulence effects. In conclusion, these findings underscore the sensitivity of the alignment between the average flame front normal **n** and the direction of the most extensive principal strain rate to the local proximity of the flame front.

4.2.5. *Flame position*

As discussed earlier, within the U-bend ($c_f/L_f \gtrapprox 0.5$), the normal velocity component is nearly zero, indicating that the flow is primarily tangential to the average flame front location. In this region, the average flame front remains steady and convex towards the reactants (Fig. 10). Together, these observations suggest that this particular flame shape coupled with hydrogen's high mass diffusion, allows non-equidiffusion effects to sustain the flame under high shear.

These effects could be linked to the non-unity Lewis number ($Le = 0.39$[1]) and preferential diffusion of hydrogen transport towards the flame front. The curved convex flame shape in the U-bend enhances this transport. This local enrichment increases the extinction strain rate, which enables combustion to persist in this region of high shear strain. For the premixed natural gas–air flame, these effects are absent due to the unity Lewis number and low diffusivity, causing the flame to extinguish under high shear conditions.

Fig. 19 shows the time-averaged flame luminescence images (300 images at 60 Hz) of a premixed hydrogen–air flame (top image: H_2%=80, $\phi = 0.4$, $Re = 11.61 \times 10^3$, $Le = 0.51$[1]) and a natural gas–air flame (bottom image: H_2%=0, $\phi = 0.7$, $Re = 3.87 \times 10^3$, $Le = 1.02$[1]). The red arrow in the top image marks the reaction zone within the U-bend for the hydrogen–air flame. In contrast, the natural gas–air flame shows no reaction in this region. However, while one-dimensional counter-flow twin premixed flame simulations (using Cantera 3.0) predict that both the hydrogen-rich flame (H_2%=80, $\phi = 0.40$) in Fig. 19 and the pure hydrogen–air flame investigated in this study (H_2%=100, $\phi = 0.35$) should extinguish at a lower strain rate than the natural gas–air flame (H_2%=0, $\phi = 0.70$), the time-averaged images in Fig. 19 show the opposite behaviour: the hydrogen-rich flame shows greater flame stability in the U-bend region compared to the natural gas–air flame. This contradicting result illustrates the limitations of one-dimensional flame simulations, which do not account for the aforementioned curvature-induced enrichment.

4.2.6. *A possible flashback path*

Given the complex geometry and unpredictable flashback behaviour, an effort was made to understand the flame's route during flashback. Prior research by Gruber et al. [24] found that with a blunt liner tip, the flame propagates along the inner liner wall, whereas with a sharp-shaped liner tip, it tends to propagate along the U-bend wall.

The lean hydrogen–air flame investigated in this study shows the ability to sustain combustion within the U-bend region, which can be

---

[1] The Lewis number is calculated as described in Altenburg et al. [9].

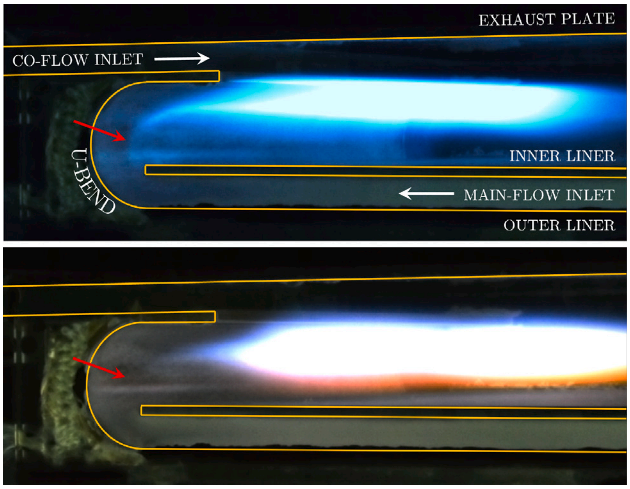

Fig. 19. Time-averaged images (300 images at 60 Hz) of a hydrogen–air flame (top) and a natural gas–air flame (bottom). The hydrogen–air flame is characterized by $H_2\% = 80$, $\phi = 0.4$, $Re = 11.61 \times 10^3$, whereas the natural gas–air flame is characterized by $H_2\% = 0$, $\phi = 0.7$, $Re = 3.87 \times 10^3$. Within the U-bend (indicated by the red arrow), a reaction zone is visible (evident from flame luminescence) for the hydrogen–air flame, which is attributed to the non-unity Lewis number effect and the preferential diffusion effect, that occurs in lean-premixed hydrogen flames due to the high mass diffusivity of hydrogen. In contrast, no reaction is observed in this region for the natural gas–air flame.

considered a flame stabilizing effect. However, downstream of the U-bend ($c_f/L_f \gtrapprox 0.5$) the shear layer weakens, resulting in increased intermittency of the flame front. This increased intermittency of the flame front is more pronounced in case R-1, operating under marginally stable flame conditions, compared to the highly stable flame case R-2, as indicated by the more diffusive flame front distribution in this region (see Fig. 10).

Although definitive conclusions regarding the flashback mechanism are challenging due to the inherent difficulties in capturing flashback events precisely in-plane using PIV measurements, the current observations suggest that flame propagation through the relatively thick boundary layer on the U-bend wall may be the route for flashback in this study. This is plausible because the greater flame intermittency in R-1 can lead to the formation of a flame bulge that reaches the low-velocity zone near the U-bend wall, resulting in an upstream propagation of the flame along that wall. Fig. 20 supports this observation, even if the in-plane occurrence of the flashback event cannot be confirmed. The figure shows a sequence of images of a flashback event captured at 286 µs time intervals (3.5 kHz image rate). The flame front shows intermittent behaviour downstream of the U-bend (images 1–3). Subsequently, the flame front approaches the U-bend wall (images 4–6) and then propagates along the U-bend wall (images 7–9). The flashback event appears to originate downstream of the highly sheared flame front, taking a route through the thick boundary layer. These insights in the most probable flashback path suggest that the thick boundary layer is prone to flashback and that extending the high shear layer with stable combustion beyond the region influenced by the boundary layer could help mitigate this risk.

5. Conclusion

This study reports on the flame stabilization and flashback of a turbulent premixed hydrogen–air flame ($\phi = 0.35$) in a trapped vortex combustor under marginally stable conditions ($Re = 9.68 \times 10^3$) and highly stable flame conditions ($Re = 13.55 \times 10^3$). The Reynolds numbers are 7.8% and 51% above the average flashback limit ($Re_{fb} = 8.98 \times 10^3$), respectively. The design of the combustor stabilizes the flame using an aerodynamically trapped vortex adjacent to the inner liner wall.

PIV measurements were conducted to investigate the flame–flow interaction by extracting the velocity field, the turbulent kinetic energy field and the strain rate field. These quantities were determined as Favre averages, and are thus suitable for a comparison with the results of numerical simulations, which typically yield Favre-averaged quantities as well.

The non-reacting cases NR-1 ($Re = 9.68 \times 10^3$) and NR-2 ($Re = 13.55 \times 10^3$) exhibit an almost identical dimensionless Favre-averaged velocity field, but the dimensionless Favre-averaged turbulent kinetic energy field is different. Both cases show vortex-shedding originating from the blunt inner liner tip. The non-reacting case NR-1 exhibits vortex shedding at a lower frequency than case NR-2. Nevertheless, the vortex structures in case NR-1 contain greater dimensionless kinetic energy compared to case NR-2 (see Fig. 9).

In the reactive cases R-1 ($Re = 9.68 \times 10^3$) and R-2 ($Re = 13.55 \times 10^3$), the average flame front is located in a region where $\widetilde{k^*}$ has a minimum. The average location of the flame front is almost identical for both Reynolds numbers.

Case R-1, operating under marginally stable flame conditions, exhibits significantly higher values of $\widetilde{k^*}$ along the average location of the flame front compared to case R-2, which corresponds to a highly stable flame (see Fig. 16). Within the U-bend ($c_f/L_f \lessapprox 0.5$), this increase can be attributed to the greater dimensionless shear strain, which could be likely linked to the difference in vortex shedding that was observed for the corresponding non-reacting cases NR-1 and NR-2. Downstream of the U-bend ($c_f/L_f \gtrapprox 0.5$), where the shear layer weakens, the higher values of $\widetilde{k^*}$ in R-1 compared to R-2 could be attributed to the increased intermittency of the flame front in R-1 (see Fig. 10). The intermittency of the flame front in this region could result in a flame bulge reaching the low-velocity zone adjacent to the U-bend wall, thereby increasing the possibility of flame flashback along the U-bend wall. This behaviour is supported by the sequence shown in Fig. 20.

For both cases, a steady, laminar-like flame front was observed within the U-bend, transitioning to a more wrinkled flame front structure further downstream. An analysis, that quantitatively examined the alignment between the strain rate and the orientation of the flame front has been conducted. Within the U-bend, the angle between the average flame front normal $\mathbf{n}$ and the direction of the most extensive strain rate $\mathbf{e}_1$ remain consistently close to 45° for both cases. This result is in agreement with the findings of Wang et al. [20], who observed the same value at the base of a premixed methane–air turbulent jet flame.

The tangential and normal velocity components along the average flame front location are analysed for both reacting cases (see Fig. 13). The results suggest that diffusion effects dominate combustion within the U-bend, where the convex-shaped flame front together with hydrogen's high mass diffusion, which leads to a non-unity Lewis number ($Le < 1$) and preferential diffusion in the hydrogen–air mixture, causes local enrichment. This enrichment increases the extinction strain rate, enabling combustion to persist in this region. The sustained combustion of the hydrogen–air within the U-bend can be considered as a stabilizing effect. Observations suggest that flashback most likely occurs through the relatively thick boundary layer on the U-bend wall, where flame intermittency can create a flame bulge that propagates upstream. These insights indicate that the thick boundary layer is prone to flashback and that extending the high shear layer with stable combustion beyond its influence could help mitigate this risk.

6. Novelty and significance

This work presents original results of experiments on a turbulent premixed hydrogen–air flame in a trapped vortex combustor. PIV measurements were conducted on a flame in a strongly curved flow field. The insights gained from this study contribute to the development of hydrogen–fueled gas turbines with improved flame stability and reduced flashback tendencies.

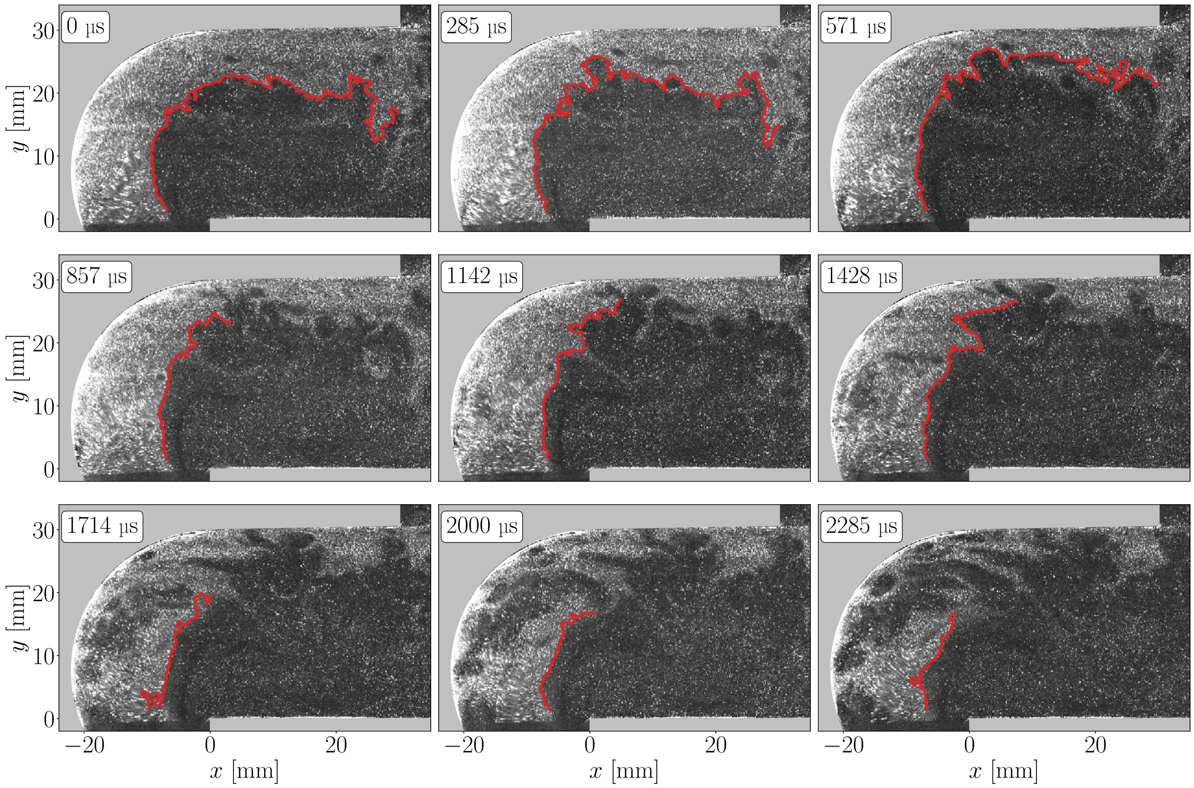

Fig. 20. A sequence of images (captured at 3.5 kHz) that illustrate a flashback event. The sequence suggests that with the blunt liner tip employed in this study, flame propagation through the relatively thick boundary layer on the U-bend wall is the route for flashback. The instantaneous flame front is indicated by the red line.

CRediT authorship contribution statement

Luuk A. Altenburg: Writing – original draft, Methodology, Investigation, Formal analysis, Conceptualization. **Sikke A. Klein:** Writing – review & editing, Supervision, Project administration, Funding acquisition, Conceptualization. **Mark J. Tummers:** Writing – review & editing, Supervision, Methodology, Formal analysis, Conceptualization.

Declaration of competing interest

The authors declare that they have no known competing financial interests or personal relationships that could have appeared to influence the work reported in this paper.

Acknowledgements

This work was funded by Rijksdienst voor Ondernemend Nederland (RVO), Netherlands under project DEI120081: High Hydrogen Gas Turbine Combustor High Pressure Test.

Appendix. Karlovitz number calculation

The pure hydrogen–air flames ($\phi = 0.35$) in this study operate at 1 atm and approximately 293.15 K (= 20 °C). At these conditions, the unstretched laminar flame speed $S_{L0} = 0.065\,\mathrm{m\,s^{-1}}$ and the thermal laminar flame thickness $\delta_L = (T_b - T_u)/(\nabla T)_{\max} = 1.513\,\mathrm{mm}$, using a one-dimensional simulation in Cantera 3.0 for a freely-propagating premixed laminar flame using the detailed reaction mechanism GRI-Mech 3.0 [25]. The Karlovitz number Ka at the main-flow inlet h_1 is evaluated as $Ka = \tau_L/\tau_\eta$, where $\tau_L = \delta_L/S_{L0}$ is the flame time scale and $\tau_\eta = \sqrt{\nu_u/\varepsilon}$, is the Kolmogorov time scale. Here, $\nu_u = 1.72 \times 10^{-5}\,\mathrm{m^2\,s^{-1}}$ is the kinematic viscosity of the unburnt mixture, calculated using Cantera 3.0, and $\varepsilon = u_o'^3/l_o$ is the turbulent dissipation rate. The turbulent velocity fluctuations u_o' were estimated using $u_o'/U_b = 0.16Re^{-1/8}$ and the corresponding integral length scale was determined as $l_o = 0.07D_H$, based on Hoferichter et al. [26]. The Damköhler number Da is evaluated as $Da = \tau_t/\tau_L$, where $\tau_t = l_o/u_o'$ is the turbulent time scale.

From the Reynolds numbers in this study $Re = U_b D_H/\nu_u = 13.55\times10^3$ (9.68×10^3), it follows that the Karlovitz number $Ka = 66$ (43) and the Damköhler number $Da = 0.10$ (0.13), which places the flames in the thin reaction zone regime of the Borghi–Peters diagram [27]. In this regime the smallest turbulent eddies are comparable or smaller than the laminar flame thickness, but much larger than the reaction zone. The eddies can therefore penetrate into the preheat zone. The reaction zone, however, retains its structure although it is wrinkled by the eddies.

References

[1] Law CK. Combustion physics. Cambridge University Press; 2010.

[2] Lieuwen T, McDonell V, Santavicca D, Sattelmayer T. Burner development and operability issues associated with steady flowing syngas fired combustors. Combust Sci Technol 2008;180(6):1169–92.

[3] Vreman AW, van Oijen JA, de Goey LPH, Bastiaans RJM. Direct numerical simulation of hydrogen addition in turbulent premixed bunsen flames using flamelet-generated manifold reduction. Int J Hydrog Energy 2009;34(6):2778–88.

[4] Bouten T, Withag J, Axelsson L-U, Koomen J, Jansen D, Stuttaford P. Development and atmospheric testing of a high hydrogen FlameSheet™ combustor for the OP16 gas turbine. In: Turbo expo: power for land, sea, and air. vol. 84942, American Society of Mechanical Engineers; 2021, V03AT04A048.

[5] Stuttaford P, Rizkalla H, Oumejjoud K, Demougeot N, Bosnoian J, Hernandez F, Yaquinto M, Mohammed AP, Terrell D, Weller R. FlameSheet™ Combustor Engine and Rig Validation for Operational and Fuel Flexibility With Low Emissions. In: Turbo expo: power for land, sea, and air. vol. 49750, American Society of Mechanical Engineers; 2016, V04AT04A040.

[6] Kakaç S, Shah RK, Aung W. Handbook of single-phase convective heat transfer. John Wiley and Sons Inc., New York, NY; 1987.

[7] Dragomir OE, Tummers MJ, Van Veen EH, Van der Heijden AEDM, Roekaerts DJEM. Experimental investigation of the HNF flame structure. Combust Flame 2008;153(1–2):149–60.
[8] Pfadler S, Beyrau F, Leipertz A. Flame front detection and characterization using conditioned particle image velocimetry (CPIV). Opt Express 2007;15(23):15444.
[9] Altenburg LA, Klein SA, Tummers MJ. Flame-induced pressure gradients in turbulent premixed natural gas-air and hydrogen-air jet flames. Combust Flame 2025;279:114314.
[10] Hunt JC, Wray AA, Moin P. Eddies, streams, and convergence zones in turbulent flows. In: Studying turbulence using numerical simulation databases. Proceedings of the 1988 sum- mer program, 2, 1988.
[11] Winoto SH, Shah DA, Mitsudharmadi H, et al. Concave surface boundary layer flows in the presence of streamwise vortices. Int J Fluid Mach Syst 2011;4(1):33–46.
[12] Schlichting H, Gersten K. Boundary-layer theory. Springer; 2016.
[13] Bradshaw P. Effects of streamline curvature on turbulent flow. Tech. rep., (AGARDograph No. 169). AGARD; 1973.
[14] Poinsot T, Veynante D. Theoretical and numerical combustion. RT Edwards, Inc.; 2005.
[15] Chakraborty N, Swaminathan N. Influence of the damköhler number on turbulence-scalar interaction in premixed flames. I. Physical insight. Phys Fluids 2007;19(4):045103.
[16] Chakraborty N, Klein M, Swaminathan N. Effects of lewis number on the reactive scalar gradient alignment with local strain rate in turbulent premixed flames. Proc Combust Inst 2009;32(1):1409–17.
[17] Steinberg AM, Driscoll JF, Swaminathan N. Statistics and dynamics of turbulence–flame alignment in premixed combustion. Combust Flame 2012;159(8):2576–88.
[18] Hartung G, Hult J, Kaminski C, Rogerson J, Swaminathan N. Effect of heat release on turbulence and scalar-turbulence interaction in premixed combustion. Phys Fluids 2008;20(3):035110.
[19] Sponfeldner T, Boxx I, Beyrau F, Hardalupas Y, Meier W, Taylor AMKP. On the alignment of fluid-dynamic principal strain-rates with the 3D flamelet-normal in a premixed turbulent V-flame. Proc Combust Inst 2015;35(2):1269–76.
[20] Wang H, Hawkes ER, Chen JH. Turbulence-flame interactions in DNS of a laboratory high karlovitz premixed turbulent jet flame. Phys Fluids 2016;28(9):095107.
[21] Cifuentes L, Dopazo C, Martin J, Jimenez C. Local flow topologies and scalar structures in a turbulent premixed flame. Phys Fluids 2014;26(6):065108.
[22] Kim SH, Pitsch H. Scalar gradient and small-scale structure in turbulent premixed combustion. Phys Fluids 2007;19(11):115104.
[23] Chu H, Berger L, Gauding M, Attili A, Pitsch H. Effects of dilatation and turbulence on tangential strain rates in premixed hydrogen and iso-octane flames. J Fluid Mech 2024;981:A5.
[24] Gruber A, Heggset T, Meyer O, Altenburg LA, Tummers MJ, Klein SA, Koomen J, Stuttaford P. Numerical and experimental investigation of a geometrically simplified, two-dimensional FlameSheet™ hydrogen burner. In: Turbo expo: power for land, sea, and air. vol. 86960, American Society of Mechanical Engineers; 2023, V03BT04A054.
[25] Smith GP, Golden DM, Frenklach M, Moriarty NW, Eiteneer B, Goldenberg M, Bowman CT, Hanson RK, Song S, Gardiner WC, Lissianski VV, Qin Z. GRI-mech 3.0. 2006.
[26] Hoferichter V. Boundary layer flashback in premixed combustion systems [Ph.D. thesis], Technische Universität München; 2017.
[27] Peters N. Turbulent combustion. Meas Sci Technol 2001;12(11):2022.